Cell Reports
Physical Science

CellPress
OPEN ACCESS

Article

Tuning crystal structure and electronic properties for enhanced oxygen intercalation pseudocapacitance in perovskite

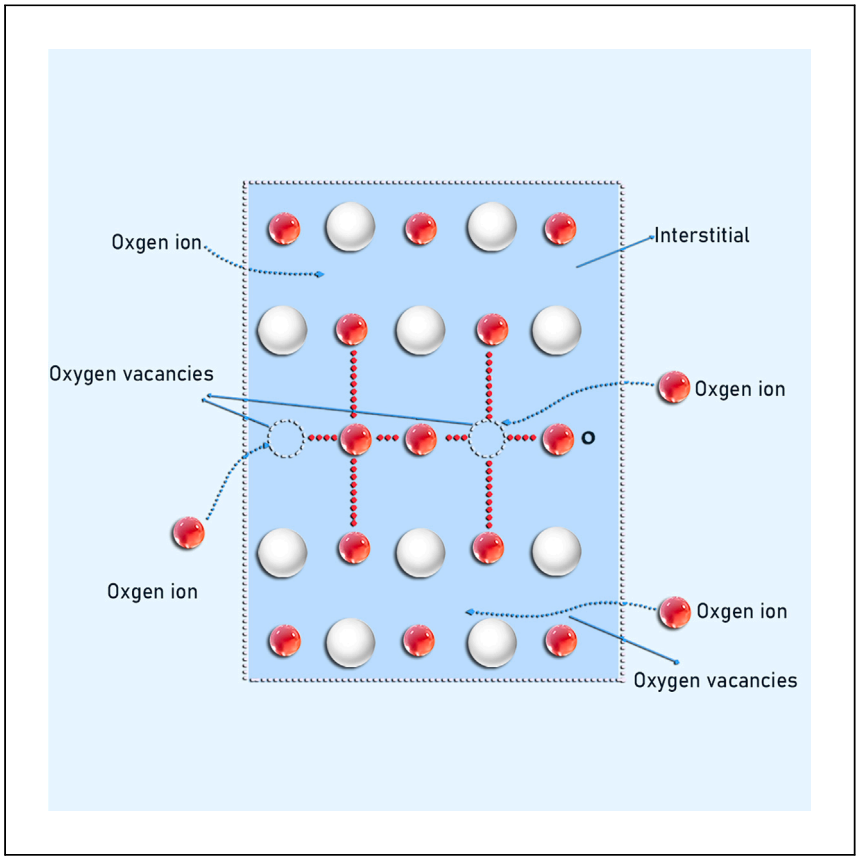

Liu et al. report that the incorporation of a layered structure markedly improves pseudocapacitance resulting from oxygen intercalation. This is achieved by introducing interstitial oxygen intercalation, which effectively overcomes the constraints imposed by oxygen vacancy concentration. Despite the rock-salt phase in the RP structure being characterized by lower electronic conductivity and oxygen vacancy concentration, A-site deficiency effectively counters these detrimental effects.

Yu Liu, Ziyang Zhu, Jiashun Wu, ..., Yujie Xu, Xinjing Zhang, Haisheng Chen

liuyu@iet.cn (Y.L.)
chen_hs@iet.cn (H.C.)

Highlights

Oxygen ions' energy storage breaks the limit of oxygen vacancy concentration

Oxygen intercalation pseudocapacitance by interstitial oxygen intercalation

Incorporation of A-site deficiency in perovskite tunes electronic properties

A new course in the design and development of materials with superior power density

Liu et al., Cell Reports Physical Science 5, 101846
March 20, 2024
https://doi.org/10.1016/j.xcrp.2024.101846

Cell Reports
Physical Science

CellPress
OPEN ACCESS

Article

Tuning crystal structure and electronic properties for enhanced oxygen intercalation pseudocapacitance in perovskite

Yu Liu,[1,2,5,*] Ziyang Zhu,[1] Jiashun Wu,[3] Zhenbin Wang,[3,4] Hualiang Zhang,[1,2] Yujie Xu,[1,2] Xinjing Zhang,[1,2] and Haisheng Chen[1,2,*]

SUMMARY

Oxygen intercalation supercapacitors with high specific capacitance and power density offer potential advantages in various applications. This study explores the potential of Ruddlesden-Popper (RP) perovskite materials for energy storage, focusing on oxygen intercalation pseudocapacitance properties. The RP structure significantly enhances oxygen intercalation pseudocapacitance by allowing interstitial oxygen intercalation, thereby overcoming limitations associated with oxygen vacancy concentration. Despite the weaker electronic conductivity and lower oxygen vacancy concentration observed in the RP structures, A-site deficiency effectively mitigates these drawbacks. $La_{0.7}Sr_{1.2}Fe_{0.9}Co_{0.1}O_4$ (rp-*d*-LSFC) exhibits a higher concentration of free electrons, leading to improved conductivity and oxygen vacancy concentrations. Consequently, rp-*d*-LSFC exhibits an excellent specific capacitance of 983.6 F g^{-1} at 1 A g^{-1}. Additionally, an asymmetric supercapacitor cell achieves an impressive energy density of 40.8 Wh kg^{-1} at a power density of 1,688.3 W kg^{-1}. Density functional theory calculations further support the above results. This work advances our understanding of oxygen intercalation pseudocapacitance mechanisms.

INTRODUCTION

Supercapacitors, also known as ultracapacitors or electric double-layer capacitors, show great promise in energy storage due to their high power density and durability. Despite advantages like low resistance and wide temperature range, their lower energy density compared to batteries limits widespread use. Addressing this, scientists explore reversible electrochemical reactions, leading to "pseudocapacitance." While the incorporation of pseudocapacitance enhances performance, it remains surface limited. Certain metal oxides offer intercalation pseudocapacitance, storing charges within bulk materials.[1] Orthorhombic Nb_2O_5 and molybdenum oxide (MoO_3) are promising for ion intercalation. MoO_3's layered structure allows easy ion intercalation, while its high conductivity enables efficient Li^+ ion intercalation.[2] Additionally, materials like TiO_2 exhibit Li^+ intercalation with minimal impact on kinetics, highlighting the importance of Li^+ ions.[3] However, this has led to an escalating demand for lithium that outpaces available supply, resulting in a global shortage. This lithium shortage is projected to occur as early as 2026, underscoring the urgency to identify alternative elements with ample reserves.[4] Alternatively, oxygen, accounting for a significant proportion of the Earth's crust and ranking high in cosmic prevalence, emerges as a promising contender. Its inherent electron affinity renders it exceptionally suitable for energy storage applications.

[1]Energy Storage Research and Development Center, Institute of Engineering Thermophysics, Chinese Academy of Sciences, Beijing 100190, P.R. China

[2]Nanjing Institute of Future Energy System, Institute of Engineering Thermophysics, Chinese Academy of Sciences, Nanjing 211100, P.R. China

[3]Department of Materials Science and Engineering, City University of Hong Kong, Hong Kong SAR 999077, P.R. China

[4]School of Energy and Environment, City University of Hong Kong, Hong Kong SAR 999077, P.R. China

[5]Lead contact

*Correspondence: liuyu@iet.cn (Y.L.), chen_hs@iet.cn (H.C.)

https://doi.org/10.1016/j.xcrp.2024.101846

Kudo et al. demonstrated a groundbreaking reversible electrochemical intercalation of oxygen ions into the $Nd_{1-x}Sr_xCoO_3$ perovskite. This phenomenon stems from filling oxygen vacancies in the perovskite oxide via intercalation of electrolyte oxygen ions. This ultimately results in the development of oxygen ion intercalation pseudocapacitance.[5] The structures of various perovskite oxides impact oxygen vacancy formation and, consequently, influence intercalation pseudocapacitive performance.[6–8] Cubic-structured perovskite oxides tend to form higher oxygen vacancies, while layered double perovskite oxides offer rapid oxygen ion diffusion channels.[9–14] An increased concentration of oxygen vacancies creates more available sites for oxygen ion intercalation, leading to higher pseudocapacitance.[6] The electrochemical properties of reduced $LaMnO_{2.91}$ and oxygen-excess $LaMnO_{3.09}$ were compared, revealing that the former exhibited a higher capacitance of 609.8 F g^{-1}.[5] This trend was also observed in our previous work on the $PrBaMn_2O_{6-\delta}$ double perovskite.[10] Establishing oxygen vacancies in perovskites is an effective means of modifying their physicochemical properties.[15] However, an excessive concentration of oxygen vacancies disrupts the delicate balance that maintains the integrity of the crystal lattice, which leads to the collapse or distortion of the perovskite crystal structure.[16] Therefore, an additional site for oxygen ions storage can effectively increase the energy density. Ruddlesden-Popper (RP) perovskite oxides with layered structures have garnered considerable attention due to their exceptional oxygen ion conductivities and electronic conductivity within the rock-salt layer.[17] RP perovskites have a general formula of $A_{n+1}B_nO_{3n+1}$, comprising A-site alkaline earth elements and B-site transition metal elements. AO rock-salt layers may exhibit anionic vacancies and/or interstitial oxygen ions, both of which result in ionic conduction. Electronic conduction can occur in perovskite-like blocks that are constructed from corner-sharing MO_6 octahedra, with M-cations occupying the center of the polyhedra and presenting multiple non-localized oxidation states. By incorporating rock-salt layers into the bulk structure, the RP exhibits enhanced performance by enabling the storage of oxide anions not only in the vacancy sites within the perovskite layers but also in the interstitial sites within the rock-salt layers.[18] Among the RP perovskite oxides, $La_{0.8}Sr_{1.2}Fe_{0.9}Co_{0.1}O_4$ (LSFC) stands out as a layered perovskite oxide with a significant concentration of oxygen vacancies. Moreover, the partial substitution of iron with cobalt has augmented its conductivity. Hence, it emerges as a promising alternative for energy storage applications.

In this study, RP perovskite oxides, $La_{0.8}Sr_{1.2}Fe_{0.9}Co_{0.1}O_4$ (rp-LSFC) and $La_{0.7}Sr_{1.2}Fe_{0.9}Co_{0.1}O_4$ (rp-*d*-LSFC), were synthesized using the EDTA-CA complex sol-gel method. The rp-LSFC characterized by the RP perovskite exhibited superior performance over a single cubic structure. The incorporation of A-site deficiency in rp-*d*-LSFC notably increased oxygen vacancy concentration and electronic conductivity, contributing to enhanced overall performance. It not only provided oxygen vacancy sites but also offered interstitial sites, which are conducive to anion intercalation. Consequently, rp-*d*-LSFC showed commendable capacity for oxygen ion intercalation pseudocapacitance. These findings offer a promising avenue for crafting tailored supercapacitor electrodes via oxygen ion intercalation. DFT (density functional theory) calculations suggested that rp-*d*-LSFC with A-site deficiency had lower oxygen vacancy formation energy and enhanced electron conductivity, improving energy storage density and expediting charge/discharge processes.

RESULTS AND DISCUSSION

Pseudocapacitive performance

The preceding research on oxygen-ion intercalation-type supercapacitors has indicated that high concentrations of oxygen vacancies, along with elevated electronic

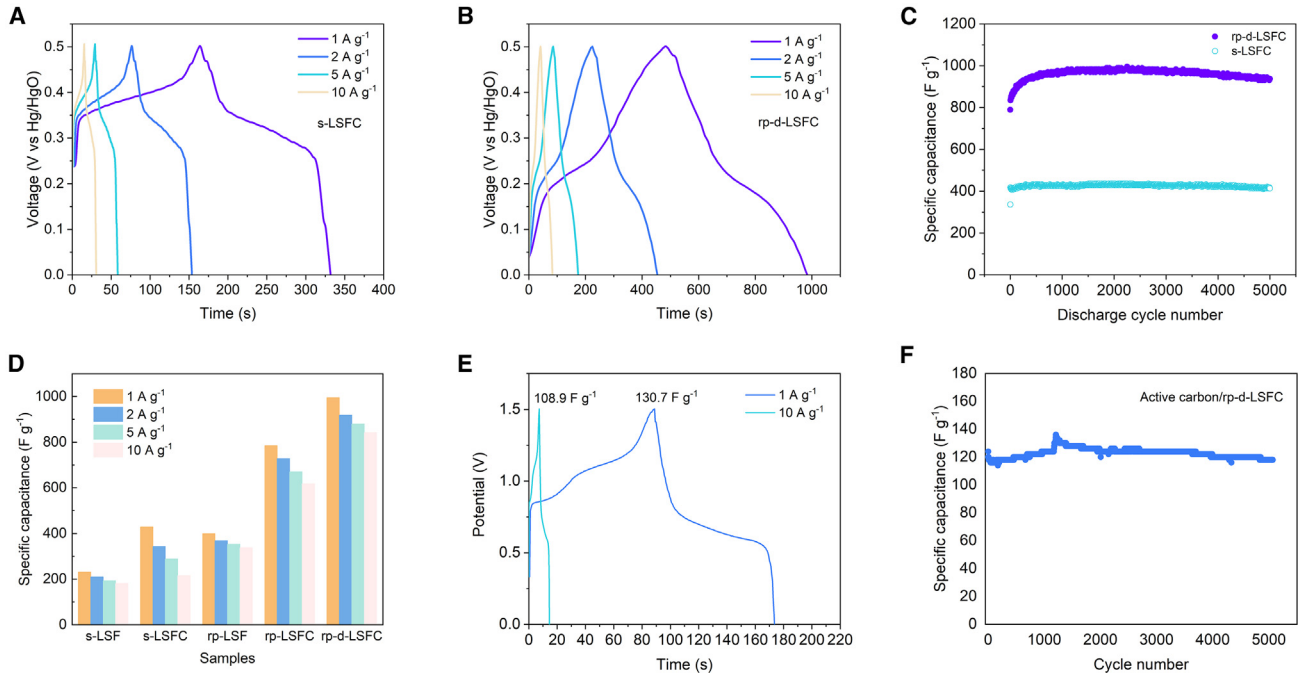

Figure 1. Oxygen intercalation-type pseudocapacitance of single perovskite and RP perovskite

(A and B) Galvanostatic charge-discharge curves of s-LSFC (A) and rp-*d*-LSFC (B) at different current densities in 6 M KOH electrolyte.

(C) Long-term cycling stability of s-LSFC and rp-*d*-LSFC electrodes at a galvanostatic charge-discharge current density of 1 A g^{-1}.

(D) The specific capacitance values of single-perovskite and RP-perovskite electrodes at different current densities in 6 M KOH electrolyte.

(E) Galvanostatic charge-discharge curves of rp-*d*-LSFC/AC ASC.

(F) Long-term cycling stability of rp-*d*-LSFC/AC ASC.

conductivity and a stable crystal structure, typically enhance specific capacitance.[6,19] This principle serves as a foundation for the design of highly efficient electrode materials. RP oxides, derivatives of perovskites, exhibit distinctive layered structures and diverse chemical compositions. Figures 1 and S1 present the galvanostatic c charge-discharge (GCD) profiles of single perovskites $La_{0.4}Sr_{0.6}FeO_3$ (s-LSF) and $La_{0.4}Sr_{0.6}Fe_{0.9}Co_{0.1}O_3$ (s-LSFC) and RP perovskites $La_{0.8}Sr_{1.2}FeO_4$ (rp-LSF), rp-LSFC, and rp-*d*-LSFC at a current density of 1 A g^{-1}. All values of potential are vs. a Hg/HgO reference electrode. The corresponding RP oxides exhibit higher specific capacitance values; for instance, rp-*d*-LSFC achieved a specific capacitance of 983.6 F g^{-1}, surpassing the 403.3 F g^{-1} achieved by the single-crystal s-LSFC. This enhancement is possibly attributed to the greater concentration of oxygen vacancies and the layered structure in RP perovskites (Figures 1A and 1B). The partial substitution of Fe with Co in rp-LSF results in a modest improvement in pseudocapacitive performance. The improvement in pseudocapacitive performance primarily stems from the heightened electrical conductivity of rp-LSFC.[20,21] However, the specific capacitance of rp-LSFC is lower than what would be estimated based on electrical conductivity, likely due to its lower oxygen vacancy concentration. The highest specific capacitance is attained by rp-*d*-LSFC with an A-site-deficient structure, registering 983.6 F g^{-1} at a current density of 1 A g^{-1}. This indicates a notable concentration of oxygen vacancies, robust electrical conductivity, and contributions from other forms of pseudocapacitance. This observation stands out significantly among oxygen ion intercalation electrodes, as achieving such high performance involves tuning electrical conductivity, crystalline structure, and oxygen vacancy concentration. Figure 1C illustrates the long-term galvanostatic discharge cycling performance of rp-*d*-LSFC and s-LSFC at a high current density of 1 A g^{-1}. Initially,

both samples undergo an activation process in the first approximately 100 cycles, attributed to the gradual increase in active sites on the electrode surface during oxygen-ion de/intercalation. This is likely a result of surface rearrangement or activity processes during continuous oxygen intercalation and deintercalation.[22] Subsequently, the specific capacitance experiences a slight decrease in the subsequent cycles. Notably, RP materials demonstrate competitive stability compared to single-perovskite materials, as depicted in Figure 1C. Both rp-LSFC and rp-*d*-LSFC exhibit higher capacity and more excellent stability performance. Specifically, rp-LSFC retains about 96.5% of its peak capacitance, while rp-*d*-LSFC maintains 92.1%, after 5,000 cycles. In contrast, single-perovskite structures display more pronounced degradation in specific capacitance during the stability test. This conspicuous disparity in cycling stability between single-perovskite structural and RP structural electrodes is primarily attributed to the negligible destruction, as the layered structure of RP perovskite mitigates significant volume changes during oxygen ion intercalation and deintercalation. Figure 1D provides an overview of the specific capacitance of all samples at different current densities.

To further validate the practical viability of rp-*d*-LSFC in enhancing supercapacitor performance, a two-electrode asymmetric supercapacitor cell was employed, utilizing active porous carbon as the anode and rp-*d*-LSFC as the cathode The cell was tested in a 6 M KOH electrolyte at ambient temperature. As illustrated in Figure 1E, a specific capacitance of 130.7 F g^{-1} was attained at 1 A g^{-1}. The durability of this two-electrode supercapacitor at 1 A g^{-1} was assessed and is depicted in Figure 1F, revealing stable specific capacitance over 5,000 cycles without notable degradation. This result underscores the excellent chemical compatibility of the perovskite cathode in rp-*d*-LSFC with the alkaline electrolyte. Under a discharging current density of 1 A g^{-1}, this two-electrode cell achieved an energy density of 40.8 Wh kg^{-1} at a power density of 1,688.3 W kg^{-1}. With a discharging current density of 10 A g^{-1}, it demonstrated superior performance, yielding an energy density of 34.1 Wh kg^{-1} at a power density of 7,672.5 W kg^{-1}. Notably, the energy density of rp-*d*-LSFC at high power densities surpasses that of other single-perovskite electrode anion intercalation supercapacitors. This phenomenon is likely attributed to its elevated conductivity and rapid oxygen diffusion rates, stemming from the heightened oxygen vacancy concentration and expanded interstitial sites. The high performance of RP perovskite electrodes, including rp-*d*-LSFC, is comprehensively examined in the subsequent sections to understand the rationale behind their superior performance.

RP perovskite characteristics

The crystallographic characteristics of all samples were detected using X-ray powder diffraction (XRD) and subsequently analyzed via the Rietveld refinement method. The results are delineated in Figures 2 and S2. The s-LSFC variant adopts a rhombohedral perovskite structure within the *R-3c* space group. The profile factor values from the refinement are provided in Table S1. In contrast, the rp-LSF, distinguished by its RP structure, exhibits a K_2NiF_4 configuration and follows the *I4/mmm* space group. Notably, materials with RP structure feature an additional rock-salt phase compared to their single-perovskite counterparts, indicative of a layered structure that possibly mitigates crystal volume fluctuations resulting from oxygen ion de/intercalation.[18] The La/Sr distribution is characterized by random occupation at the (0,0,z) site, with Fe positioned at the (0,0,0) site and oxygen distributed across the (0.5,0,0) O1 and (0,0,zo) O2 sites. Upon substituting Fe with Co, the same K_2NiF_4 structure is maintained, preserving the space group *I4/mmm*. An observable shift in the XRD peak position of rp-LSFC toward lower diffraction angles suggests unit cell shrinkage, a consequence of the smaller Co ion radius compared to Fe

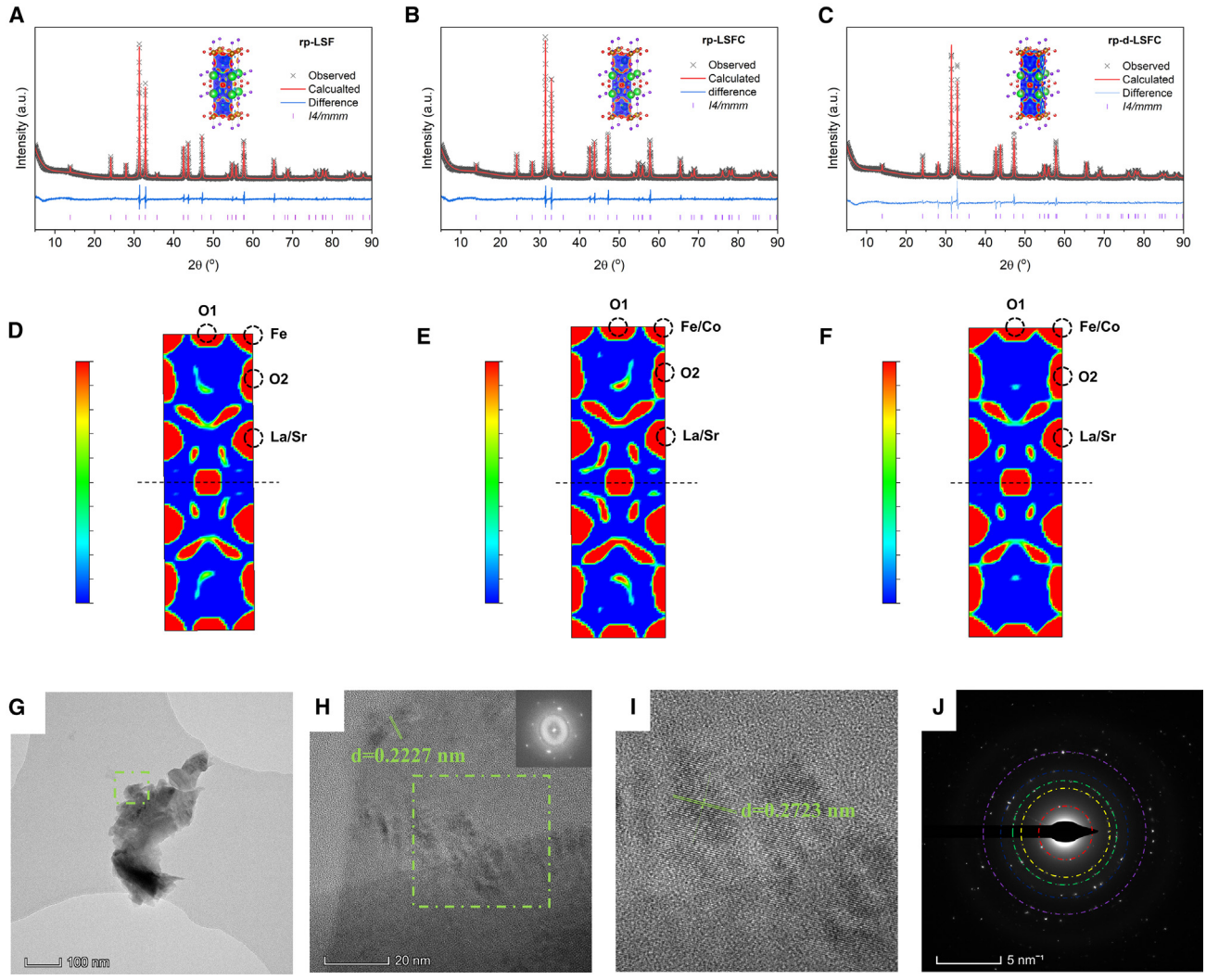

Figure 2. Phase structure and microstructure of single and RP perovskites

(A–C) X-ray diffraction spectra and Rietveld refinement results of rp-LSF (A), rp-LSFC (B), and rp-*d*-LSFC (C). All of them possess a K_2NiF_4 structure and space group *I4/mmm*.

(D–F) Electron density maps of rp-LSF (D), rp-LSFC (E), and rp-*d*-LSFC (F) obtained from Fourier transforms (FTs) of XRD Rietveld refinement results.

(G) High-resolution TEM (HR-TEM) image of rp-*d*-LSFC, which displays the morphology of a particle.

(H and I) HR-TEM image of rp-*d*-LSFC with two different interplanar spacing and fast FT (FFT) patterns.

(J) Selected-area electron diffraction pattern of rp-*d*-LSFC.

ions.[23] Even with the partial removal of La to achieve an A-site-deficient structure in rp-*d*-LSFC, the *I4/mmm* space group remains conserved. The shift in peak positions is attributed to the partial A-site vacancy, indicating structural changes. It is conventionally held that oxygen ion intercalation occurs within the perovskite lattice to occupy oxygen vacancies.[5] Consequently, specific capacitance is bounded by the restricted oxygen vacancy concentration, as an excess of such vacancies could lead to the collapse of the perovskite crystal phase.[19] In comparison to densely packed crystal structures like s-LSF, the 2D-layered architecture of rp-LSF, encompassing rock-salt and perovskite layers, contributes to its higher specific capacitance due to additional interstitial oxygen ion intercalation.[18] The electrical conductivity of perovskite materials is pivotal in determining the viability of oxygen ion intercalation supercapacitors for high-current charging-discharging cycles and effective energy

utilization.[24] However, perovskite electrical conductivity is intrinsically limited by perovskites' semi-conductor properties. Incorporating Co as a dopant has been demonstrated to enhance perovskite conductivity. The electron density maps derived from lattice planes via Fourier transformation of XRD refinement results revealed alterations in the distribution of electron density around metal–oxygen bonds upon Co introduction. Specifically, the broader overlap between oxygen 2p and transition metal 3d orbitals engenders heightened electronic conductivity.[25] This electron density was found to be augmented around the O1–Fe/Co bond in A-site-deficient rp-*d*-LSFC compared to rp-LSF and rp-LSFC, indicating heightened electron mobility between the two atoms. This heightened electron density could potentially facilitate electron migration, reducing redox reaction barriers and enhancing overall electrochemical performance.[26–28] Additionally, the bond lengths between Fe/Co and oxygen were examined, revealing longer bond lengths corresponding to lower bond energies, which favor electronic conductivity. For example, the Fe–O bond lengths in rp-LSF and rp-LSFC are measured at 1.921 and 1.927 Å, respectively. In the case of Co–O bonds, the lengths are 1.927 Å for rp-LSFC and 2.095 Å for rp-*d*-LSFC. A greater bond length (M–O) correlates with lower bond energy, which is conducive to enhanced electronic conductivity. However, the introduction of Co as a dopant, while enhancing electronic conductivity, also leads to a reduction in oxygen vacancy concentration, thereby diminishing the pseudocapacitance associated with oxygen ion intercalation.

The perovskite oxides were obtained through sintering precursors at 1,000°C. The morphological characteristics of the synthesized perovskite oxides were initially examined using scanning electron microscopy. As depicted in Figure S3, the images of s-LSF and s-LSFC consist of bulk particles with diameters ranging from 200 to 600 nm. The size of s-LSFC particles is slightly larger compared to s-LSF without Co doping, suggesting that cobalt can enhance agglomeration and grain growth. Similarly, RP-structured perovskites, namely rp-LSF, rp-LSFC, and rp-*d*-LSFC, exhibit similar bulk particle morphologies ranging from 300 to 800 nm. These samples present smooth surfaces without evident pore structures. Transmission electron microscopy (TEM) was also employed to examine the morphologies and crystal structures of the perovskite oxides. The average particle size of these samples was estimated to be approximately 500 nm. High-resolution TEM was used for further investigations. Both s-LSF and s-LSFC (Figure S4) revealed single-perovskite crystallites. They exhibited clear crystal fringes with interplanar spacings of about 0.1935 nm corresponding to (204) and 0.2233 nm corresponding to (202), respectively. However, as illustrated in Figures 2 and S4, the RP perovskites, namely rp-LSF, rp-LSFC, and rp-*d*-LSFC, displayed crystallites that simultaneously exhibited characteristics of both RP and single-perovskite units. For example, rp-*d*-LSFC exhibited two different interplanar spacings of about 0.2227 and 2723 nm, aligning with the distances of the (105) and (110) crystal planes for the rock-salt and perovskite phases, respectively. Specific surface area measurements were conducted using N_2 adsorption-desorption techniques and calculated through the Brunauer-Emmett-Teller method, with results detailed in Table S2. These samples showed comparable specific surface areas, suggesting that all single- and RP-perovskite samples share nearly identical morphologies and possess similar numbers of active reaction sites for oxygen-ion intercalation on their surfaces.

The oxygen vacancy concentrations in all samples were initially assessed through XRD refinement, with results presented in Figure 3A. To obtain more precise values for oxygen vacancies, iodometric titration was also employed for measurement (Figure 3A). While the titration results indicated slightly lower values compared to those

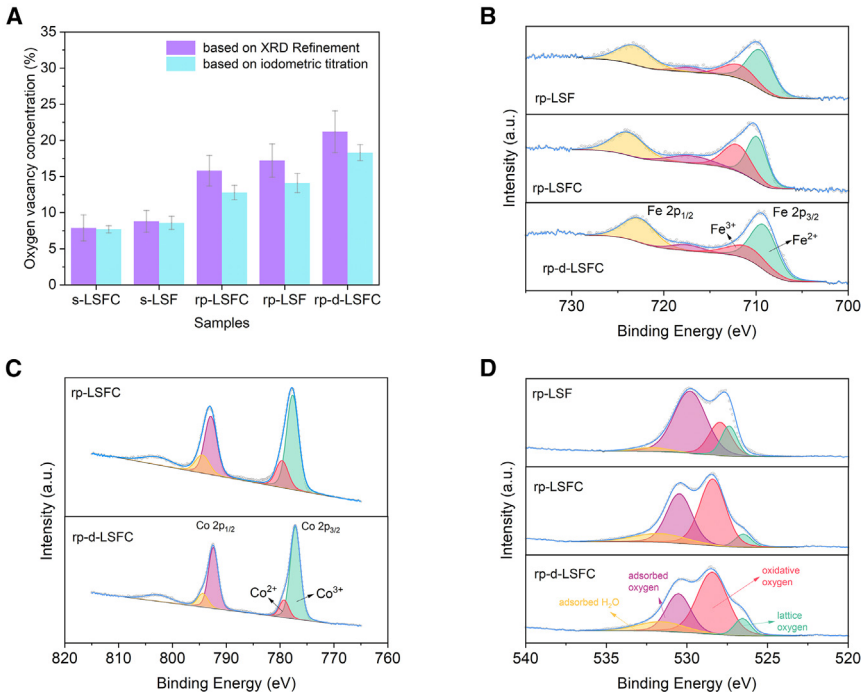

Figure 3. Oxygen vacancies and surface chemical state of RP perovskite

(A) Oxygen vacancy concentrations of perovskites based on the XRD refinement results and iodometric titration.

(B–D) High-resolution Fe 2p (B), Co 2p (C), and O1s (D) XPS spectra of perovskite.

The error bar is defined as the average of three relative errors between the experimental averages and the experimental values.

obtained from XRD refinement, both methods displayed a similar trend in variation with composition and component. rp-LSF exhibited a marginally lower oxygen vacancy concentration compared to s-LSF, suggesting that single perovskites possess a higher quantity of oxygen vacancies than RP perovskites. This implies that the majority of oxygen defects in rp-LSF exist in the form of oxygen interstitials, which may have implications for the material's properties.[29] The Co doping strategy led to a reduced number of oxygen vacancies in s-LSFC, limiting its capacitive behavior during charge-discharge measurements. Therefore, it is imperative to devise an optimal approach that simultaneously maximizes the concentration of oxygen vacancies and electronic conductivity in rp-LSFC. To address this, an A-site-deficient structure was created through defect engineering, effectively enhancing the oxygen vacancy concentration in rp-*d*-LSFC. rp-*d*-LSFC exhibited an oxygen vacancy concentration of 18.3, surpassing the 7.9 observed in rp-LSCF. Consequently, the enhanced pseudocapacitive performance of rp-*d*-LSFC primarily stems from the augmented oxygen vacancies and electronic conductivity, achieved by tuning the electronic structure of the perovskites. Although rp-LSFC possesses a lower oxygen vacancy concentration compared to s-LSFC, it demonstrates a higher capacity. This is primarily attributed to the specific capacitance of rp-LSFC, which predominantly arises from the contribution of oxygen ions inserting into interstitial positions. This scenario similarly applies to samples rp-LSF and s-LSF.

The chemical state of surface elements across all samples was assessed using X-ray photoelectron spectroscopy (XPS). Figures 3 and S5 present the XPS results, revealing the valence states of Co and Fe, which play a pivotal role in inducing redox

pseudocapacitance during oxygen ion intercalation. It is evident that both Fe and Co exist in multiple valence states on the perovskite oxides' surfaces, including Fe^{2+}/Fe^{3+} and Co^{2+}/Co^{3+}, indicating the dynamic nature of redox reactions during oxygen ion intercalation.[30,31] In Figure S5, Fe spectra for s-LSF exhibit a comparable ratio of Fe^{2+} and Fe^{3+}. Conversely, RP and Co-doped rp-LSFC reveal a higher ratio of Fe^{3+} in comparison to s-LSF (Figure 3B). The A-site-deficient perovskite structure also enhances the ratio of Co^{3+}, as depicted in Figure 3C, suggesting a correlation between A-site deficiency and increased Co^{3+} valence states. Co doping and A-site deficiency induce a slight shift of the Fe peak toward lower binding energy, indicating a weakening of the Fe–O bond. La displays two chemical states of La $3d_{5/2}$ with binding energies around 834.1 and 850.7 eV, while Sr exhibits three chemical states of Sr $3d_{5/2}$ with binding energies at around 130.6, 132.4, and 134.5 eV across all samples (Figure S5). Introduction of Co leads to shifts in binding energies of La and Sr toward lower energy, signifying a marginal reduction in the metal–oxygen bond energy due to cobalt's slightly higher electronegativity.[32] Figure 3D illustrates the O1s spectra in rp-*d*-LSFC, revealing characteristic peaks corresponding to adsorbed water (H_2O, 532.7 eV), adsorbed oxygen (OH^-/O_2, 530.4 eV), highly oxidative oxygen (O_2^{-2}/O, 528.6 eV), and lattice oxygen (O^{2-}, 528.0 eV). These peaks are also discernible in the O1s spectra of rp-LSF and rp-LSFC. Quantitative assessment of the various oxygen species in different samples is presented in Figure S5. rp-LSF demonstrates a higher ratio of O^{2-} on the surface compared to s-LSF, underscoring the notable capacity for retaining lattice oxygen in the layered structure. This is analogous to the phenomenon observed between s-LSFC and rp-LSFC where the RP structure significantly contributes to lattice oxygen retention. Calculation of surface oxygen vacancy concentration on the perovskite was performed based on the relative areas of O_2^{-2}/O peaks. The values of 10.7, 9.1, and 18.7 for rp-LSF, rp-LSFC, and rp-*d*-LSFC, respectively, signify that surface oxygen vacancies hold greater significance than those within the material's bulk. Notably, rp-*d*-LSFC exhibits the highest relative concentration of O_2^{-2}/O species on the surface, indicating a substantial creation of surface oxygen vacancies through A-site cation deficiency.[33] As established in prior studies, oxygen vacancies serve not only as sites for oxygen ion intercalation within the crystal lattice but also expedite the oxygen diffusion process.[5] Furthermore, the interstitial space in rock-salt-layered structural oxides further enhances capacitance through lattice oxygen ion intercalation.[18] Therefore, the augmented pseudocapacitance in the rp-LSFC electrode can be attributed to several contributing factors. Firstly, the distinctive layered crystalline structure provides additional pseudocapacitance through interstitial oxygen ion intercalation. Secondly, Co doping enhances electrical conductivity owing to the weaker metaloxygen bond. Thirdly, A-site deficiency leads to a higher oxygen vacancy concentration. Fourthly, the larger unit cell volume confers a highly stable crystalline structure.

Electrochemical kinetics

In light of the growing demand for highly active bifunctional perovskites characterized by elevated oxygen vacancy concentration and electronic conductivity, particularly in the context of advancing energy storage technology, there exists a pronounced need to engineer bifunctional perovskites capable of exhibiting substantial oxygen-ion intercalation pseudocapacitance throughout the charge-discharge process. To investigate the electrochemical anion intercalation behavior of all samples, cyclic voltammetry (CV) was conducted at varying scan rates within a three-electrode system. This setup comprised a working electrode, a Hg/HgO reference electrode, and a Pt counter electrode, employing a 6 M KOH electrolyte. Figures 4 and S6 present the CV curves for all samples recorded at different scan rates. Notably, as scan rates decrease, the redox reaction peaks in the CV

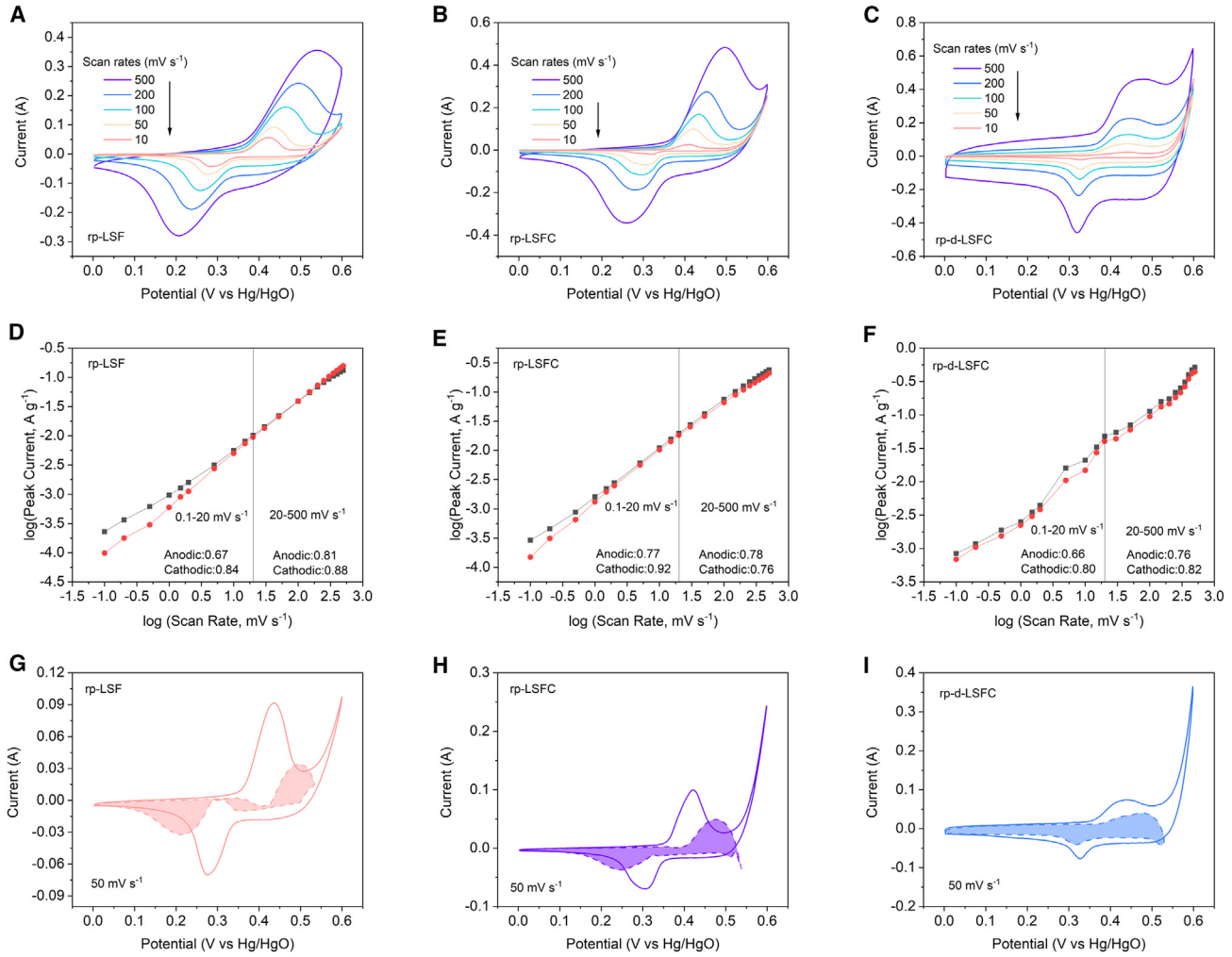

Figure 4. Kinetic analysis of the electrochemical behavior of RP perovskite

(A–C) Cyclic voltammetry (CV) plots of rp-LSF (A), rp-LSFC (B), and rp-*d*-LSFC (C) electrodes at a range of scan rates in a potential window of 0.0–0.6 V in a 6 M KOH electrolyte.

(D–F) Peak current value of CV vs. $v^{-1/2}$ curves of rp-LSF (D), rp-LSFC (E), and rp-*d*-LSFC (F) electrodes.

(G–I) CV in 6 M KOH at 50 mV s^{-1} with the charge transfer kinetics contributions in the shaded envelope shown for rp-LSF (G), rp-LSFC (H), and rp-*d*-LSFC (I) electrodes.

profiles shift toward lower potential, owing to the extended interaction time between electrolyte ions and active species within the samples, enhancing the reversibility of the redox process. Each of the samples exhibits a pair of weak/strong redox peaks in the CV curves, indicative of a reversible redox reaction associated with $Co^{2+}/Co^{3+}/Co^{4+}$ and Fe^{2+}/Fe^{3+} (occurring near 0.5 V vs. Hg/HgO), making a substantial contribution. Additionally, the specific capacitance of perovskite oxides can be estimated from the area enclosed by the corresponding CV curve, as detailed in Table S3. It is evident that rp-*d*-LSFC demonstrates the highest specific capacitance among all samples at a uniform scan rate of 50 mV s^{-1}. Notably, s-LSCF exhibits a greater capacity than s-LSF, underscoring the enhanced conductivity of the perovskite following Co doping. Moreover, the specific capacitance values derived from CV are marginally lower than those from GCD, implying that the specific capacitance of a perovskite is contingent on the charge-discharge rate.

The energy storage mechanism induced by oxygen intercalation and oxygen diffusion in RP perovskites has been subject to further investigation. During the intercalation process, oxygen ions assume the form of OH^- on the surface of perovskite oxide in the KOH electrolyte, followed by O^{2-} diffusion into the bulk lattice of the electrodes.[34] Hence, it is crucial to determine whether oxygen ion intercalation into the perovskite electrodes is primarily influenced by surface phenomena or by diffusion within the lattice. CV testing was conducted on all samples at various scan rates, with the peak current and scan rate of CV adhering to the power-law relationship:

$$I = av^b.$$

The b value in this equation is regarded as indicative of the contribution fraction from semi-infinite linear diffusion (b = 0.5) and surface capacitive mechanisms (b = 1). Plots of log(i) and log(v) for both anodic and cathodic peaks were examined (Figures 4D–4F and S7). In the case of s-LSFC, the b values for anodic and cathodic peaks ranged from 0.66 to 0.80 at slow scan rates and from 0.76 to 0.82 at faster scan rates. However, rp-*d*-LSFC exhibited b values ranging from 0.68 to 0.74 for anodic peaks and from 0.64 to 0.77 for cathodic peaks, indicating that the kinetics of rp-*d*-LSFC predominantly follow a semi-infinite linear diffusion process. Similar behavior was observed in other RP structure perovskites, signifying a diffusion-limited process. Consequently, there are two oxygen ion intercalation processes contributing to the overall intercalation pseudocapacitance: oxygen ion intercalation into oxygen vacancy sites and oxygen ion intercalation into interstitial sites. The relative contribution of capacitive and diffusion-controlled intercalation mechanisms was assessed using the following equation:

$$I(V) = k_1(v) + k_2(v)^{1/2}$$

The values of $k_1(v)$ and $k_2(v)^{1/2}$ delineate the current contributions from capacitive and diffusion-controlled intercalation mechanisms, respectively. This allowed for the determination of the proportion of different processes (Figures 4G–4I and S8). Subsequently, it was established that rp-*d*-LSFC and rp-LSFC are kinetically limited, primarily exhibiting capacitive behavior due to the rapid lattice oxygen diffusion kinetics. Conversely, s-LSFC and s-LSF predominantly manifest surface capacitive behavior across the entire voltage window, indicating only oxygen ion intercalation into the oxygen vacancy site. To further delve into the oxygen ion intercalation kinetics of single-perovskite and RP-perovskite electrodes, the rates of oxygen ion intercalation and deintercalation diffusion were assessed for all these samples. The diffusion rates were determined at the oxidation potential or reduction potential of Fe or Co ions, respectively. Notably, rp-*d*-LSFC exhibited the highest overall intercalation oxygen diffusion rates of 8.69×10^{-11} $cm^2\ s^{-1}$ and deintercalation diffusion rates of 4.35×10^{-11} $cm^2\ s^{-1}$ (Table S4). This remarkable diffusion rate can be attributed to the elevated oxygen vacancy concentration and electron conductivity resulting from the defective A-site structure and Co dopant. In contrast, rp-LSF demonstrated a lower oxygen diffusion compared to s-LSFC, potentially attributable to the relatively stronger metal–oxygen bond prior to Co doping into the lattice.

First-principles calculations

To elucidate the robust energy storage capabilities of deficient RP materials exemplified by rp-*d*-LSFC, DFT calculations were conducted employing the structural models in Figure S9. The formation energy of oxygen vacancies plays a pivotal role in gauging the oxygen vacancy concentration in metal oxides. This process can be envisaged as the rupture of metal–oxygen bonds. The assessment of these energies thus facilitates a data-informed exploration of promising materials for

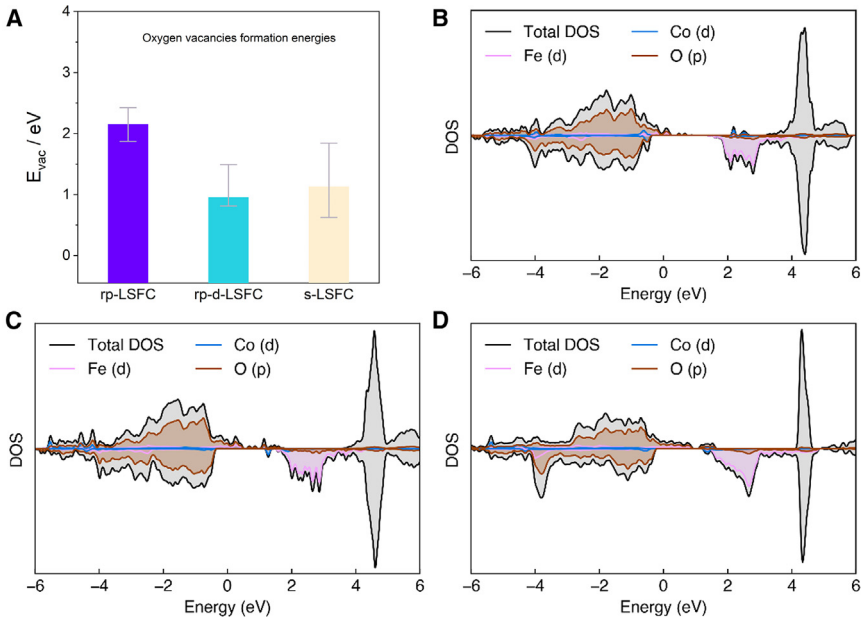

Figure 5. DFT calculation for formation energy of oxygen vacancies (E_{vac}) and density of states (DOS)

(A) Calculated E_{vac} of rp-LSFC, rp-*d*-LSFC, and s-LSFC. The histogram displays the average values of E_{vac}. The error bar represents the distribution of calculated E_{vac} for distinct oxygen sites.
(B–D) Calculated DOS for perovskite rp-LSFC (B), rp-*d*-LSFC (C), and s-LSFC (D).

oxygen intercalation pseudocapacitance. As depicted in Figure 5A, rp-*d*-LSFC exhibits the lowest oxygen vacancy formation energy among these three samples, confirming its high oxygen vacancy concentration. This finding highlights that the A-site-deficient structure favors the formation of oxygen vacancies, in contrast to the RP-layered structure, which exhibits the opposite effect. Moreover, to gain deeper insights into how A-site deficiency and RP structure influence the electronic properties, we calculated the density of states of s-LSFC, rp-LSFC, and rp-*d*-LSFC using DFT calculations, as shown in Figures 5B–5D. When compared to Figures 5B and 5C, the introduction of A-site deficiency markedly enhances the electronic states near the Fermi level, thereby improving the electrical conductivity. Notably, a significant density of electronic states is also observed around the Fermi level for s-LSFC (Figure 5D), which implies a conductivity akin to that of rp-*d*-LSFC. These observations are consistent with the results of our experimental results.

In summary, a variety of single-perovskite and RP-perovskite oxides were successfully synthesized via sol-gel reaction, demonstrating remarkable efficacy in electrochemical energy storage. Experimental analysis revealed that the introduction of a layered structure significantly enhances oxygen intercalation pseudocapacitance by including interstitial oxygen intercalation, thereby overcoming limitations imposed by oxygen vacancy concentration. Despite the weaker electronic conductivity and lower oxygen vacancy concentration associated with the rock-salt phase in the RP structure, A-site deficiency effectively mitigates these adverse effects. The observed higher concentration of freely moving electrons around the O1-Fe/Co bond in rp-*d*-LSFC attests to the tailored electronic structure, resulting not only in heightened conductivity but also in a favorable oxygen vacancy concentration. These materials exhibit kinetic limitation, predominantly showcasing capacitive behavior due to rapid lattice oxygen diffusion kinetics. Consequently, the rp-*d*-LSFC

electrode achieves an outstanding specific capacitance of 983.6 F g^{-1} at 1 A g^{-1}. Meanwhile, the asymmetric supercapacitor cell, comprising an active porous carbon anode and an rp-*d*-LSFC cathode, attains an energy density of 40.8 Wh kg^{-1} at a power density of 1,688.3 W kg^{-1}. Furthermore, DFT calculations indicate that A-site deficiency fosters the generation of oxygen vacancies and augments electronic conductivity. Thus, this study not only charts a new course in the design and development of materials with superior power density and volumetric energy density through the manipulation of crystal lattice and electronic structure but also advances our comprehension of the mechanisms underpinning oxygen intercalation pseudocapacitance.

EXPERIMENTAL PROCEDURES

Resource availability

Lead contact

Further information and requests for data and resources should be directed to and be fulfilled by the lead contact, Yu Liu (liuyu@iet.cn).

Materials availability

This study did not generate new unique reagents.

Data and code availability

This study did not generate/analyze datasets and code.

Details of synthesis, characterization, and analysis

The details of materials synthesis, basic characterization, electrochemical measurements, and DFT computation are provided in the supplemental experimental procedures.

SUPPLEMENTAL INFORMATION

Supplemental information can be found online at https://doi.org/10.1016/j.xcrp.2024.101846.

ACKNOWLEDGMENTS

Y.L. acknowledges support by the National Natural Science Foundation of China under award number no. 52202324. This work is also supported by the Hundred Talents Program of the Chinese Academy of Sciences (CAS). The CAS Nanjing Future Energy System Research Institute independently deploys research project E3550101. Z.W. acknowledges the funding support from City University of Hong Kong Start-up Grant 9020004. The calculations were carried out using the computational facilities at CityU Burgundy, managed and provided by the Computing Service Centre at City University of Hong Kong. X.Z. is thankful for the support from Beijing Natural Science Foundation JQ21010.

AUTHOR CONTRIBUTIONS

Y.L. and H.C. conceived this project. Y.L. and Z.Z. performed the materials preparation and characterization and electrochemical testing. J.W and Z.W. performed the DFT calculation. H.Z., Y.X., and X.Z. performed the powder diffraction and XPS. Y.L. wrote the manuscript. All authors discussed the results and commented on the manuscript.

DECLARATION OF INTERESTS

The authors declare no competing interests.

Received: November 17, 2023
Revised: December 21, 2023
Accepted: February 1, 2024
Published: February 28, 2024

REFERENCES

1. Augustyn, V., Come, J., Lowe, M.A., Kim, J.W., Taberna, P.-L., Tolbert, S.H., Abruña, H.D., Simon, P., and Dunn, B. (2013). High-rate electrochemical energy storage through Li+ intercalation pseudocapacitance. Nat. Mater. *12*, 518–522. https://doi.org/10.1038/nmat3601.

2. Xiao, X., Peng, Z., Chen, C., Zhang, C., Beidaghi, M., Yang, Z., Wu, N., Huang, Y., Miao, L., Gogotsi, Y., and Zhou, J. (2014). Freestanding MoO3−x nanobelt/carbon nanotube films for Li-ion intercalation pseudocapacitors. Nano Energy *9*, 355–363. https://doi.org/10.1016/j.nanoen.2014.08.001.

3. Han, J., Hirata, A., Du, J., Ito, Y., Fujita, T., Kohara, S., Ina, T., and Chen, M. (2018). Intercalation pseudocapacitance of amorphous titanium dioxide@nanoporous graphene for high-rate and large-capacity energy storage. Nano Energy *49*, 354–362. https://doi.org/10.1016/j.nanoen.2018.04.063.

4. Liu, B., Zhang, Q., Liu, J., Hao, Y., Tang, Y., and Li, Y. (2022). The impacts of critical metal shortage on China's electric vehicle industry development and countermeasure policies. Energy *248*, 123646. https://doi.org/10.1016/j.energy.2022.123646.

5. Mefford, J.T., Hardin, W.G., Dai, S., Johnston, K.P., and Stevenson, K.J. (2014). Anion charge storage through oxygen intercalation in LaMnO3 perovskite pseudocapacitor electrodes. Nat. Mater. *13*, 726–732. https://doi.org/10.1038/nmat4000.

6. Liu, Y., Jiang, S.P., and Shao, Z. (2020). Intercalation pseudocapacitance in electrochemical energy storage: recent advances in fundamental understanding and materials development. Materials Today Advances *7*, 100072. https://doi.org/10.1016/j.mtadv.2020.100072.

7. Guo, G., Ouyang, K., Yu, J., Liu, Y., Feng, S., and Wei, M. (2020). Facile Synthesis of LaCoO3 with a High Oxygen Vacancy Concentration by the Plasma Etching Technique for High-Performance Oxygen Ion Intercalation Pseudocapacitors. ACS Appl. Energy Mater. *3*, 300–308. https://doi.org/10.1021/acsaem.9b01558.

8. Tomar, A.K., Joshi, A., Atri, S., Singh, G., and Sharma, R.K. (2020). Zero-Dimensional Ordered Sr2CoMoO6-δ Double Perovskite as High-Rate Anion Intercalation Pseudocapacitance. ACS Appl. Mater. Interfaces *12*, 15128–15137. https://doi.org/10.1021/acsami.9b22766.

9. Liu, Y., Ran, R., Li, S., Jiao, Y., Tade, M.O., and Shao, Z. (2014). Significant performance enhancement of yttrium-doped barium cerate proton conductor as electrolyte for solid oxide fuel cells through a Pd ingress–egress approach. J. Power Sources *257*, 308–318. https://doi.org/10.1016/j.jpowsour.2014.02.013.

10. Liu, Y., Wang, Z., Veder, J.-P.M., Xu, Z., Zhong, Y., Zhou, W., Tade, M.O., Wang, S., and Shao, Z. (2018). Highly Defective Layered Double Perovskite Oxide for Efficient Energy Storage via Reversible Pseudocapacitive Oxygen-Anion Intercalation. Adv. Energy Mater. *8*, 1702604. https://doi.org/10.1002/aenm.201702604.

11. Choi, S., Yoo, S., Kim, J., Park, S., Jun, A., Sengodan, S., Kim, J., Shin, J., Jeong, H.Y., Choi, Y., et al. (2013). Highly efficient and robust cathode materials for low-temperature solid oxide fuel cells: PrBa0.5Sr0.5 Co2−xFexO5+δ. Sci. Rep. *3*, 2426. https://doi.org/10.1038/srep02426.

12. Chroneos, A., Yildiz, B., Tarancón, A., Parfitt, D., and Kilner, J.A. (2011). Oxygen diffusion in solid oxide fuel cell cathode and electrolyte materials: mechanistic insights from atomistic simulations. Energy Environ. Sci. *4*, 2774–2789. https://doi.org/10.1039/C0EE00717J.

13. Liang, T., Zhang, X., Su, L., Hou, R., Yang, B., Lang, J., Yang, S., and Yan, X. (2022). Superiority of Cubic Perovskites Oxides with Strong B-O Hybridization for Oxygen-Anion Intercalation Pseudocapacitance. Adv. Funct. Mater. *32*, 2202245. https://doi.org/10.1002/adfm.202202245.

14. Liang, T., Hou, R., Zhang, X., Yang, B., Yang, B., Yang, S., Zhang, X., and Yan, X. (2023). Spintronic State-Induced Interface Reconfiguration of 2H-Perovskite Related Oxides for Pseudocapacitance Increase. Adv. Funct. Mater. *33*, 2302272. https://doi.org/10.1002/adfm.202302272.

15. Ji, Q., Bi, L., Zhang, J., Cao, H., and Zhao, X.S. (2020). The role of oxygen vacancies of ABO3 perovskite oxides in the oxygen reduction reaction. Energy Environ. Sci. *13*, 1408–1428. https://doi.org/10.1039/D0EE00092B.

16. Tyunina, M., Pacherova, O., Kocourek, T., and Dejneka, A. (2021). Anisotropic chemical expansion due to oxygen vacancies in perovskite films. Sci. Rep. *11*, 15247. https://doi.org/10.1038/s41598-021-93968-1.

17. Zhu, Y., Lin, Q., Hu, Z., Chen, Y., Yin, Y., Tahini, H.A., Lin, H.-J., Chen, C.-T., Zhang, X., Shao, Z., and Wang, H. (2020). Self-Assembled Ruddlesden–Popper/Perovskite Hybrid with Lattice-Oxygen Activation as a Superior Oxygen Evolution Electrocatalyst. Small *16*, 2001204. https://doi.org/10.1002/smll.202001204.

18. Forslund, R.P., Pender, J., Alexander, C.T., Johnston, K.P., and Stevenson, K.J. (2019). Comparison of perovskite and perovskite derivatives for use in anion-based pseudocapacitor applications. J. Mater. Chem. A Mater. *7*, 21222–21231. https://doi.org/10.1039/C9TA06094D.

19. Liu, Y., Wang, Z., Zhong, Y., Xu, X., Veder, J.-P.M., Rowles, M.R., Saunders, M., Ran, R., and Shao, Z. (2020). Activation-free supercapacitor electrode based on surface-modified Sr2CoMo1-xNixO6-δ perovskite. Chem. Eng. J. *390*, 124645. https://doi.org/10.1016/j.cej.2020.124645.

20. Xie, Y., Lu, K., Duan, J., Jiang, Y., Hu, L., Liu, T., Zhou, Y., and Hu, B. (2018). Enhancing Photovoltaic Performance of Inverted Planar Perovskite Solar Cells by Cobalt-Doped Nickel Oxide Hole Transport Layer. ACS Appl. Mater. Interfaces *10*, 14153–14159. https://doi.org/10.1021/acsami.8b01683.

21. Deng, Z., Zhang, G.-g., Liu, W., Peng, D.-k., and Chen, C.-s. (2002). Phase composition, oxidation state and electrical conductivity of. Solid State Ionics *152–153*, 735–739. https://doi.org/10.1016/S0167-2738(02)00317-X.

22. Liu, Y., Dinh, J., Tade, M.O., and Shao, Z. (2016). Design of Perovskite Oxides as Anion-Intercalation-Type Electrodes for Supercapacitors: Cation Leaching Effect. ACS Appl. Mater. Interfaces *8*, 23774–23783. https://doi.org/10.1021/acsami.6b08634.

23. Shannon, R.D., and Prewitt, C.T. (1970). Revised values of effective ionic radii. Acta Crystallogr. B *26*, 1046–1048. https://doi.org/10.1107/S0567740870003576.

24. Li, H., Guo, H., Huang, K., Liu, B., Zhang, C., Chen, X., Xu, X., and Yang, J. (2018). Carbon electrode with conductivity improvement using silver nanowires for high-performance supercapacitor. Appl. Phys. *124*, 763. https://doi.org/10.1007/s00339-018-2182-4.

25. Gao, L., Tang, C., Liu, J., He, L., Wang, H., Ke, Z., Li, W., Jiang, C., He, D., Cheng, L., and Xiao, X. (2021). Oxygen Vacancy-induced Electron Density Tuning of Fe3O4 for Enhanced Oxygen Evolution Catalysis. Energy Environ. Mater. *4*, 392–398. https://doi.org/10.1002/eem2.12112.

26. Yabuuchi, N., Nakayama, M., Takeuchi, M., Komaba, S., Hashimoto, Y., Mukai, T., Shiiba, H., Sato, K., Kobayashi, Y., Nakao, A., et al. (2016). Origin of stabilization and destabilization in solid-state redox reaction of oxide ions for lithium-ion batteries. Nat. Commun. *7*, 13814. https://doi.org/10.1038/ncomms13814.

27. Zhao, P., Jiang, Y., Tang, Z., Li, Y., Sun, B., Wu, Y., Wu, J., Liu, Y., and Bu, W. (2021). Constructing Electron Levers in Perovskite Nanocrystals to Regulate the Local Electron Density for Intensive Chemodynamic Therapy. Angew. Chem., Int. Ed. Engl. *60*, 8905–8912. https://doi.org/10.1002/anie.202100864.

28. Kim, D., Cho, M., and Cho, K. (2017). Rational Design of Na(Li1/3Mn2/3)O2 Operated by Anionic Redox Reactions for Advanced Sodium-Ion Batteries. Adv. Mater. *29*, 1701788. https://doi.org/10.1002/adma.201701788.

29. Yang, L., Jiao, Y., Xu, X., Pan, Y., Su, C., Duan, X., Sun, H., Liu, S., Wang, S., and Shao, Z. (2022). Superstructures with Atomic-Level Arranged Perovskite and Oxide Layers for Advanced Oxidation with an Enhanced Non-Free Radical Pathway. ACS Sustain. Chem. Eng. *10*, 1899–1909. https://doi.org/10.1021/acssuschemeng.1c07605.

30. Kalasina, S., Kongsawatvoragul, K., Phattharasupakun, N., Phattharaphuti, P., and Sawangphruk, M. (2020). Cobalt oxysulphide/hydroxide nanosheets with dual properties based on electrochromism and a charge storage mechanism. RSC Adv. *10*, 14154–14160. https://doi.org/10.1039/D0RA01714K.

31. Li, P., Xuan, Y., Jiang, B., Zhang, S., and Xia, C. (2022). Hollow La0.6Sr0.4Ni0.2Fe0.75 Mo0.05O3-δ electrodes with exsolved FeNi3 in quasi-symmetrical solid oxide electrolysis cells for direct CO2 electrolysis. Electrochem. Commun. *134*, 107188. https://doi.org/10.1016/j.elecom.2021.107188.

32. Papac, M., Stevanović, V., Zakutayev, A., and O'Hayre, R. (2021). Triple ionic–electronic conducting oxides for next-generation electrochemical devices. Nat. Mater. *20*, 301–313. https://doi.org/10.1038/s41563-020-00854-8.

33. Zhu, Y., Zhou, W., Yu, J., Chen, Y., Liu, M., and Shao, Z. (2016). Enhancing Electrocatalytic Activity of Perovskite Oxides by Tuning Cation Deficiency for Oxygen Reduction and Evolution Reactions. Chem. Mater. *28*, 1691–1697. https://doi.org/10.1021/acs.chemmater.5b04457.

34. Wang, W., Xu, X., Liu, Y., Zhong, Y., and Shao, Z. (2018). Rational Design of Metal Oxide–Based Cathodes for Efficient Dye-Sensitized Solar Cells. Adv. Energy Mater. *8*, 1800172. https://doi.org/10.1002/aenm.201800172.